Tissue architectural cues drive the emergence of non-random trafficking of human tumor cells in the larval zebrafish.

Colin D. Paul[a], Kevin Bishop[b], Alexus Devine[a], William J. Wulftange[c], Elliott L. Paine[a], Jack. R. Staunton[a], Steven Shema[d], Val Bliskovsky[d], Lisa M. Miller Jenkins[a], Nicole Y. Morgan[c], Raman Sood[b], and Kandice Tanner[a*]

[a]Laboratory of Cell Biology, Center for Cancer Research, National Cancer Institute, National Institutes of Health

[b]Zebrafish Core, Translational and Functional Genomics Branch, National Human Genome Research Institute, National Institutes of Health

[c]National Institute of Biomedical Imaging and Bioengineering, National Institutes of Health

[d] CCR Genomics Core, Center for Cancer Research, National Cancer Institute, National Institutes of Health

* Corresponding author information: Dr. Kandice Tanner; Center for Cancer Research, National Cancer Institute, Building 37, Room 2132, Bethesda, MD 20892; Ph: 260-760-6882; Email: kandice.tanner@nih.gov

Keywords: Cancer metastasis; organotropism; extravasation; organ intravital imaging; confined cell migration; topographical cues; tissue mechanics; tissue architecture

ABSTRACT

Sites of metastasis are non-random, with certain types of cancers showing a preference of distal organ colonization. One fundamental question is what drives the emergence of organ selectivity. We determined that human breast tumor cells that home to specific murine organs migrated similarly within the circulatory system but ultimately colonized different organs in larval fish. Brain seeking clones homed preferentially to the brain, whereas bone seeking clones preferentially homed to the hematopoietic tissue in the tail (analogous to fetal mammalian bone marrow). Microenvironmental cues such as tissue mechanics and architecture are important regulators of tumorigenesis. We hypothesized that the physical properties of the tissue and vessel architecture drive the emergence of non-random targeting in the larval fish. We determined that vessel widths in the larval fish are on the scale of human capillaries with diverse architectures: ordered within the brain to disordered within the hematopoietic tissue. Both clones were occluded in each organ analog, where greater numbers accumulated in disordered blood vessels for organs that share similar tissue mechanics. Organ selectivity was an emergent phenomenon observed by 120 h post-injection following cell arrest. Functional blocking of integrin signaling redirected targeting of the bone-seeking clones. Our results show that specificity is driven by both occlusion and extravasation at the tumor-endothelial interface, in part regulated by integrin signaling and the vessel architecture.

INTRODUCTION

Metastasis describes the process whereby cancer cells move from a primary tumor and establish lesions in distinct organs(1-3). Metastasis is non-random, with differences in organ targeting and clinical latency correlated with initial tumor type in line with Paget's seed and soil hypothesis(1-4). Differences in tumor targeting and latency following dissemination are critical for the treatment of certain types of cancer(3, 5-7). For example, breast cancer cells can disseminate through the circulation prior to the primary tumor reaching a clinically detectable size, and latent disseminated cells can lead to re-emergence of aggressive cancers up to ~20 years following initial treatment(6). Therefore, understanding how cells target specific organs, whether differences exist in this targeting, and the factors critical to cell survival following dissemination are critical for developing treatments for metastatic and refractory cancers.

At the time of diagnosis of the primary tumor, it would be ideal to know *a priori* what organs would be favorable to disseminated cells. A limited repertoire of isogenic clones exists such that multiple organ-seeking clones are derived from the same parental clone within the same strain of mouse(1, 8, 9). From these model systems, cell ("seed") intrinsic differences in genes and signaling pathways that regulate organ specificity have been evaluated(1, 8, 9). A number of methods exist that permit study of tumor cell dissemination from the primary site and evaluation of the abundance of circulating tumor cells present in the bloodstream(10-13). However, the mechanisms that determine how cells transition from the circulation to successfully colonize the "soil" at distant organs is less understood, particularly in the context of the earliest stages of metastasis and simultaneously in multiple organs. In addition to intrinsic genetics, the microenvironment has emerged as a potent regulator of tumor cell fate(7, 12, 14). We thus

hypothesized that differences in the transition of cells from the bloodstream to the parenchyma of distinct tissues with different microenvironmental properties may be particularly important to organ specificity.

Tumor cells along the metastatic cascade encounter different physical microenvironments during capillary arrest and extravasation into organs(15, 16). We asked at what stage can non-random organ targeting be first determined? However, these steps in early colonization are rare and difficult to study using current models(17). The zebrafish is rapidly becoming a model for studying tumor behavior at different stages of the metastatic cascade(18-20). Continuous imaging of the entire larval fish allows for the visualization of single cells within multiple organs. We hypothesized that microenvironment composition, mechanics, and architecture of diverse organs are sufficiently conserved across vertebrates, thus allowing us to evaluate what physical cues may drive organ targeting.

Here, we determined that brain- or bone-targeting human breast tumor cells showed non-random organ targeting following direct injection into the zebrafish circulation. Vessel architecture was a key determinant of initial cell distribution following circulatory dissemination, and differences in architecture caused both breast cancer cell lines to preferentially occlude in the zebrafish caudal vascular plexus (CVP; analog for mammalian bone marrow) vs. the zebrafish brain. Interestingly, both clones became occluded in the zebrafish brain and CVP at equal frequencies, with similar average residence times in each organ. Additional organ preference differentiating the cell lines emerged at the time of extravasation, where impaired ability of brain-targeting cells to extravasate in the CVP led to an increase in relative brain colonization by these cells. Overall, these data suggest that patterns of metastatic spread are driven, at least in part, by different patterns of both cell occlusion and extravasation during early metastatic dissemination.

RESULTS

Organotropic human tumor cells show non-random distal organ colonization in a zebrafish model of metastasis

Organs that are frequent sites of metastasis in human patients are well conserved between mammals and zebrafish(21, 22). As early as the first few days after fertilization, key components of the zebrafish brain, central nervous system (CNS), and hematopoietic niche have emerged and are functional(22-25). Therefore, we reasoned that human tumor cells that home to murine organs(8, 9) may also show a non-random dissemination and survival in larval zebrafish. We introduced sub clones of MDA-MB-231 human breast adenocarcinoma cells that were selected for their potential to home to murine brain (denoted 231BR) and bone (denoted 231BO)(8) to the zebrafish circulatory system and asked if these cell lines would also show a non-random organ specificity in larval fish following early organ colonization (**Figure 1A**). Strikingly, 231BR and 231BO cells homed to the zebrafish brain and caudal vascular plexus (CVP; mammalian fetal liver counterpart), respectively, 5 days after direct injection into the circulation via the dorsal aorta **(Figures 1A-D, G).** In mammals, the fetal liver is the embryonic equivalent of the adult bone marrow. Non-random targeting was also observed in sub clones of $HER2^{+}$ Bt474m1 human breast cancer cells. In that case, brain-targeting Bt474m1-Br3 cells(9) were found to be enriched in the brain compared to the parental Bt474m1 cells at 1 day post-injection (dpi; **Figures 1E-F, H).**

Having observed distinct organ targeting of 231BR and 231BO cells, we next asked if these observed differences were due simply to differences in survival in the tissue parenchyma at a

particular metastatic site. Thus, we co-injected both clones directly into the brain of optically transparent Casper zebrafish **(Figures 1I-J).** We determined via both longitudinal imaging of the same fish (**Figure 1K**) and sampling of fish from the injected cohort at different time points (**Supplementary Figure 1A-C**) that both clones showed similar survival for one week within the brain parenchyma. To confirm that survival of the bone-tropic clone was not due to cytokines or physical presence of the brain tropic clone, we also performed injection of a single clone into the brain, where we observed that both 231BR and 231BO cells exhibited robust and similar cell survival in the brain **(Supplementary Figure 1D-F)**. Thus, we determined that differences in 231BR and 231BO organ targeting were not due simply to differences in cell survival or proliferation in the tissue parenchyma.

Capillary arrest within multiple organs is regulated by vessel architecture and is not due to differences in cell migration.

The metastatic cascade involves cell invasion or shedding into the circulatory system, arrest in the capillaries of target organs, extravasation into the parenchyma of these organs, and either dormancy or proliferation to establish a secondary lesion(15, 16). In mammalian systems, microenvironmental cues such as tumor-stromal crosstalk are important regulators of disseminated tumor outgrowth(7, 14, 26). Hence, organ selectivity may emerge at different stages of the cascade. Thus, we asked if differences between 231BR and 231BO cells are first observed when cells are migrating within the circulatory system at sites of eventual arrest to determine how early cell trafficking could impact eventual tissue selectivity. We identified three areas of transit relevant to colonization of the brain and CVP: blood vessels in the CVP, brain, and intersegmental vessels (ISV**) (Figure 2A).** To confirm that capillary arrest can be evaluated at this stage of development

(2 days post fertilization (dpf)), we measured vessel diameters in the brain and ISV, which averaged 9.9±2.4 and 10.6±2.6 µm, respectively, and ranged from ~5-15 µm in width **(Figures 2A-C).** Remarkably, these distributions are similar to human lung and nailbed capillaries and are similar to those seen in mice, rats, and rabbits(27-31). Although the sinusoidal vessel structure of the CVP at 2 dpf prevented accurate characterization of local vessel diameter **(Figure 2A),** the vascular network of entire fish can be likened to human capillary beds relevant to the arrest of human cancer cells.

Having confirmed the utility of the zebrafish model for evaluating cell arrest in multiple organs, we injected fluorescently labeled 231BO or 231BR cells into the zebrafish circulation and simultaneously imaged cell trafficking in the brain and CVP. Injection via the dorsal aorta led to cell dispersal throughout the vasculature (**Supplementary Figure 2**). Intravital imaging began from ~4-6 h after injection and continued for the subsequent 12 h. On average, an equal number of cells passed through the brain and CVP (normalized per fish, where both organs could be imaged), indicating that any observed differences in cell speed or occlusion were not driven by unequal exposure to cells during their movement through the circulation (**Figure 2D**). Tracking of cell movement in 3D through vessels in the zebrafish brain and CVP revealed that cells moved at greater average speeds within the lumen of vessels in the brain than within the CVP for both clones, where the organ of observation was a statistically significant source of variation in cell speed by two-way ANOVA **(Figures 2A, E,F; Supplementary Videos 1-4)**. Observed speeds were several orders of magnitude less than the blood velocity in embryonic zebrafish(32) and were not due to zebrafish growth, which was corrected for using 3D image registration (**Supplementary Figure 3**). For cells trafficking within these organ analogs, we next measured the residence time representative of capillary arrest. The residence time of both clones was significantly greater in the

CVP than in the brain, where the organ of interest but not cell type was the significant source of variation by two-way ANOVA **(Figure 2G)**. Generally, a majority of cells quickly (<3 h) passed through the vasculature and moved out of frame, though a subset of long-resident cells was present in both organs, especially in the CVP **(Figure 2H)**. One concern may be that the signaling cues that drive cross talk between host and tumor cells may not be fully conserved in the human-zebrafish xenograft system. Thus, we fabricated in vitro microchannel mimetics that recreated vessel widths but where the luminal spaces were coated with human extracellular matrix (ECM) proteins (**Supplementary Figure 4, Supplementary Video 5**). Comparison of cell migration in vivo within zebrafish ISVs and the geometric in vitro mimetics revealed that both clones showed similar motilities (**Figure 2I-L**). Interestingly, motility was largely independent of the type of ECM protein used to coat the microchannels (**Figure 2L**). Thus, we reasoned that vessel width was the determinant of cell motility and that observed cell speeds were not due to host stromal signaling abnormalities (**Figure 2I-L**).

Organ selectivity is determined at the tumor-endothelial interface in zebrafish

Within a given organ, tissue architecture, composition, and regulatory signaling networks provide cues that span length and timescales to drive the emergence of a metastatic lesion(15, 33). Confident that there were no differences in cell migration between 231BR and 231BO cells to these organs, we asked if any cell that is occluded would then extravasate based on the physical cues it received at that site. We observed organ selectivity occurring in two phases, one providing an early partitioning between the brain and CVP that was independent of cell type and the second differentiating 231BR and 231BO cells. First, we found that a greater number of cells for each clone was arrested in the vessels found within the CVP compared to those found in the brain

(**Figure 3A-B**). To better understand preferential arrest in the CVP, we examined both the topographical and mechanical properties of vessels in the brain and CVP. At the single cell level, a cell senses its environment using protrusions that may span a few microns (filopodia) to roughly the diameter of a cell (blebs and lamellopodia). Thus, to determine what a cell would sense, we calculated an order parameter(34) describing tortuosity of the vessel on the length scale corresponding to roughly that of a cell diameter (20 µm; see also **Supplementary Figure 5**). The order parameter in the highly oriented intersegmental vessels dorsal to the CVP was close to 1, while the order parameter was significantly lower in the CVP compared to both the head and intersegmental vessels. Thus, the ISVs were the most ordered, whereas the CVP vessels had the greatest tortuosity and the brain vessels showed intermittent order **(Figure 3C).** Functionally, the physical environment around the cell is also characterized by microenvironmental mechanics. We next sought to characterize the tissue mechanics within each organ. We employed in *vivo* optical-trap-based active microrheology to measure tissue mechanics (35-37). At 2 dpf, there is no significant difference as a function of organ, however, at 4 dpf the CVP is significantly stiffer (150%) than the brain at that age **(Figure 3D-E).** Thus, the stiffness of the zebrafish brain and CVP are nearly identical at the time of cell injection at 2 dpf, while the sinusoidal vessel organization of the CVP is topographically distinct from that of the brain, leading to preferential cell arrest in the CVP independently of cell type.

We next set out to examine the rate-limiting steps conferring organ selectivity in the zebrafish model. Simply, if a cell becomes "stuck," are there cell-line specific advantages in extravasation at a given organ? Longitudinal imaging of fish injected with human cancer cells at 3, 4 and 7 dpf (1, 2, 5 dpi) revealed that 231BR cells occluded in the CVP were unable to extravasate efficiently and were partially cleared by 5 dpi (**Figure 3F**). In contrast, 231BO cells

exhibited high rates of extravasation and survival in the CVP (**Figure 3F**). While extravasation was occasionally observed to occur by 1 dpi (**Supplementary Videos 6,7**), we observed that cells typically extravasated between 2-5 dpi after remaining in the vessel lumen for at least 24 h. Quantification of the percentage of cells present at 5 dpi that had extravasated in the CVP indicated significantly greater extravasation of 231BO than 231BR cells (**Figure 3G**). Thus, differences in extravasation potential in the CVP drove the second phase of organ selectivity, with decreased extravasation of 231BR cells in the CVP causing an increase in the relative number of 231BR cells in the brain of the zebrafish. This lead to the differences in organ targeting observed by 5 dpi (**Figure 1G**).

Extravasation is mediated by β1 integrin in the CVP

We next sought to determine the underlying driver of organ specificity. We reasoned that each clone may interpret physical cues differently, as extravasation in the topographically complex vessels of the CVP was the primary driver of differential organ targeting between 231BR and 231BO cells. RNAseq analysis indicated a number of differences between 231BR and 231BO cells, with 1,297 of 28,261 identified genes being significantly differentially expressed, including a number of genes involved with focal adhesion formation and cell contractility (**Figure 4A**). To better understand the proteins expressed by the cells during metastatic colonization, we performed label-free mass spectrometry on each cell line. The differentially regulated proteins between the cell lines included mechanosensory and adhesion proteins (**Figure 4B**), as well as serpin B2, which has been implicated in brain metastasis (**Supplementary Figure 6**). Pathway analysis of mass spectrometry data revealed that a number of pathways involving integrins and focal adhesions associated with mechanosensing were upregulated in 231BO compared to 231BR cells (**Figure**

4C). Of the pathways on this list, β1 integrin emerged as a key integration point involved in the majority of the pathways (**Figure 4C**). Importantly, β1 integrin has been implicated as one of the key proteins for cell fate decisions on time scales spanning hrs.-days when cells encounter a new environment(38, 39). Thus, we reasoned that modulating β1 integrin activity in the first 24 hours may be sufficient to skew capillary arrest for each clone. As observed in previous experiments, cells remained largely rounded and within the vasculature immediately following injection for cells treated with both an IgG control and β1 integrin function blocking antibody (**Figure 4D-J**). Interestingly, modulation of β1 integrin reduced arrest time of 231BO at the brain, while little differences were seen in the less mechanosensitive 231BR cells or in the topographically complex CVP (**Figure 4H,J, Supplementary Video 8**). Moreover, treatment of 231BO cells with the function blocking antibody tended to skew arrest of these cells away from the head and towards the CVP compared to control cells treated with an antibody against mouse IgG (**Figure 4J**). These data suggest that in the topographically complex environment of the CVP, cell trapping and occlusion is the primary driver of arrest. In contrast, integrin-dependent adhesion is more necessary in the more linear brain microvasculature, so modulation of integrin activity more greatly effects the more mechanosensitive 231BO cells in that organ.

DISCUSSION

Tumor cells encounter a myriad of environmental cues along the metastatic cascade before eventual arrest and outgrowth in a secondary organ(15, 16). While mechanisms of cell escape from a primary tumor have been well characterized (40, 41), visualization of the exit from the circulatory system at the latter stages of the cascade are less understood. Moreover, the mechanisms which drive organ selectivity, particularly during early metastasis, are not well characterized. Here, we employed a zebrafish model to study dissemination of human tumor cells

and eventual colonization in a developmental stage at which the vasculature had properties comparable to tissue properties of mammalian capillary beds. Intravital imaging of human organotropic cell lines revealed that these cells also displayed non-random colonization of zebrafish organs over a period of 5 days after injection (**Figure 5A**). In the first phase of organ selectivity, cells disseminated preferentially to the zebrafish CVP, which had vasculature with increased topographical complexity compared to the brain vasculature (**Figure 5B**). This pattern of dissemination was dependent, at least to some degree, on the function of β1 integrin. While this stage of dissemination provided organ selectivity in that sense that cells were non-randomly dispersed to different organs, there was no difference observed between the bone-targeting and brain-targeting cell lines used. For these cell lines, the second phase of organ selectivity was an emergent phenomenon, with extravasation mediating selectivity at the CVP (**Figure 5C**). Following this stage of selectivity, brain-seeking clones colonized the larval brain at greater rates than bone-seeking clones, which preferred the caudal venous plexus (CVP), the fetal equivalent of the bone marrow niche (**Figure 1G, Figure 5C**). This work emphasizes the importance of the interplay between tissue architecture and cell behavior at the vascular interface to drive preferential colonization of one organ at early stages of metastasis.

Metastatic lesions are mostly located in organs that are outside the range of single cell imaging techniques. One advantage of the fish is the ability to image the whole organism whilst maintaining single cell resolution not readily achieved in the murine systems where multi organ sensitivity is needed. In line with Paget's hypothesis, the "soil" contributes to the efficacy of the establishment of a distant lesion. Two pairs of isogenic organotropic clones, (MDA-MB-231 and BT474 derived) displayed non-random targeting in the larval fish **(Figure 1).** In a recent study, homing of patient derived and cell lines for multiple myeloma to the CVP was observed within a

few minutes after injection(42). Here, we observed differential targeting for non-hematological cancers. Moreover, we observe that organ specificity occurred at different times following dissemination, where it can be observed between 1-5 days post injection. Within this window, cells are able to survive and in a limited capacity proliferate in the presence of the innate immune system before adaptive immunity has emerged(43). In the larval fish, brain architecture and cell type are conserved at the developmental stage that was used. However, at this stage, osteoclasts are not fully mature; instead, the CVP is analogous to the hematopoietic stem cell (HSC) niche, both of which contain sinusoidal vascular vessels, fibroblastic reticular cell networks, and perivascular hematopoietic stem and progenitor cells (23, 44-46). Moreover, the cytokines implicated in maintaining the niche, such as CXCR4-CXCL12, are conserved between zebrafish and mammals(23, 47). In mammalian systems, tumor conditioned HSCs have been implicated in increased metastasis(48). Thus, we reasoned that "bone tropic" clones favored the CVP in response to similar cues. Interestingly, the metastatic efficiency – an indicator of how many cells survive dissemination to exit and colonize – is comparable or greater than what has been observed in murine studies(49). These results suggest that there is sufficient homology to study initial trafficking steps in multiple organs not readily accessible in some studies. In the zebrafish model, ~100 cells are introduced into each fish; thus, it may be possible to screen possible metastatic sites at the time of diagnosis with patient derived tissue.

Circulating tumor cells are continuously shed into the circulation system comprised of differential flows and vessel architectures(16). The use of transgenic fish also permits the visualization of key aspects of tumor-capillary dynamics that are not readily created using in vitro mimetics **(Figure 2).** Within the fish, a broad diversity of vessel widths and architectures with differential blood flow can be used to interrogate the role of the physical microenvironment.

Within the CVP, vessel architecture is comparable to the tortuosity found within bone marrow, which is distinct from the organized linear blood vessels observed at other organs(44-46). Continuous tracking of multiple cells revealed that cells are move at speeds well below blood flow(32) and comparable to those of zebrafish macrophages (50). Interestingly, both organotropic clones exhibited similar motility within confined environments in an in vitro system(51, 52).These data suggest that topographical cues dictate cell motility when vessel widths are comparable to cell sizes. We confirm that the organ analogs are also similar to each other on the day of injection and that the tissue mechanics are similar to 3D hydrogel mimetics(35, 37, 53, 54). Furthermore, initial trafficking within the capillaries were similar, where greater numbers of cells were arrested in the CVP. Here, the tortuous nature of the underlying architecture is sufficient to drive increased occlusion.

Extravasation of cancer cells at secondary sites occurs predominantly within capillary beds and is thought to be a key step in the metastatic cascade to initiate metastatic lesion formation(1). In this model, extravasation was seen to be the rate limiting step in conveying organ selectivity between 231BR and 231BO cells. Differences in proteins implicated in mechanosensing were observed for the tumor cell “seeds” (55). Of these proteins, β1integrin has been implicated in modulating extravasation for multiple types of tumors using in vivo and in vitro assays(19, 56). Here, we show that not only is it differentially regulated between clones, but also that function blocking of the antibody primarily affected cell occlusion in the more linear brain vessels compared to the tortuous CVP and had a greater effect on the bone-tropic clone, which had greater endogenous β1 integrin expression. Previous studies have shown that Twist expression regulates β1dependent extravasation(19). Recently, exosomes implicated in priming distant lesions showed distinct integrin expression patterns for specific organs such as the lung and liver(57).

Interestingly, in that system, exosomes harvested from bone tropic cells induced vascular leakiness but with a limited repertoire of integrins(57). Here, our results suggest that organotropic clones may express similar proteins but use specific strategies for organ targeting. Taken together, these data suggest that the interplay between tissue architecture and integrin profile may drive non - random extravasation in the zebrafish. These findings suggest that the larval fish possess physiological similarities that may be used to screen potential metastatic sites using patient derived cells.

ACKNOWLEDGEMENTS

This research was supported by the Intramural Research Program of the National Institutes of Health, the National Cancer Institute. The MDA-MB-231 clones were a kind gift of Professor Toshiyuki Yoneda (Indiana University-Purdue University). The Bt474m1 clones were a kind gift from Professor Dihua Yu (Univ. of TX, MD Anderson Cancer Center). All of the transgenic zebrafish lines were kindly provided by Dr. Brant Weinstein, NICHD, NIH. We thank Dan Castranova, Jian Liu and Blake Carrington for useful discussions. We would like to thank Susan Garfield and Langston Lim, CCR Confocal Microscopy Core Facility, Laboratory of Cancer Biology and Genetics, NCI for use of the core microscopes.

AUTHOR CONTRIBUTIONS

K.T., L.J, V.B., R.S., N.M. designed experiments, C.P., K.T., K.B., A.D., J.S., W.W., E.P., S.S., performed experiments, C.P., K.T., K.B., A.D., J.S., W.W.,E.P.,S.S., V.B. performed data analysis. K.T., C.P., N.M. wrote the main manuscript text. C.P, K.T., J.S, W.W. prepared figures. All authors reviewed the manuscript.

COMPETING FINANCIAL INTERESTS STATEMENT

The authors declare no competing financial interests.

MATERIALS & CORRESPONDENCE

Correspondence and material requests should be addressed to Kandice Tanner, Ph.D., 37 Convent Dr., Bethesda, MD 20852. Email: kandice.tanner@nih.gov.

MATERIALS AND METHODS

Zebrafish husbandry

Animal studies were conducted under protocols approved by the National Cancer Institute and the National Institutes of Health Animal Care and Use Committee. Zebrafish were maintained at 28.5°C on a 14-hour light/10-hour dark cycle according to standard procedures. Embryos were obtained from natural spawning, raised at 28.5°C, and maintained in fish water (60 mg Instant Ocean© sea salt per liter of DI water). Embryos were checked regularly for normal development. For all experiments, embryos were transferred to fish water supplemented with N-phenylthiourea (PTU; Sigma P7629-25G) between 18-22 hpf to inhibit melanin formation and maintain optical transparency. PTU water was prepared by dissolving 16 µl of PTU stock (7.5% w/v in DMSO) per 40 µl of fish water. Water was replaced daily. For cancer cell injections, embryos were maintained at 28.5°C until the time of injection (48 h) and kept at 33°C following injection as previously described. Injected fish were maintained at 33°C until reaching 4 dpf and were then introduced to a larger zebrafish housing system and held in water at 28.5°C. Regular feeding commenced at 5 dpf.

Zebrafish lines

For analysis of non-random tissue targeting of MDA-MB-231 and Bt474 cell lines, the recently described Tg(MRC1a:EGFP/flk:mCherry) zebrafish was used(58). In this transgenic strain, EGFP is expressed under the MRC1a promoter to label, at the larval stage, the venous circulation, while mCherry is expressed under the flk promoter to label the vasculature. For analysis of the zebrafish vasculature (vessel size and organization) and measurement of cell migration speeds through the intersegmental vessels, 2 dpf Tg(fli:EGFP) transgenic fish were used. The Tg(fli:EGFP) strain(59) was also used in experiments studying the effects of treatment with β1-integrin function blocking antibodies on initial cell trafficking through the vasculature.

Cell culture

MDA-MB-231 bone tropic (231BO) and brain tropic (231BR) cells were grown and maintained in high glucose (4.5 g/l) DMEM containing 10% FBS, 1% L-glut, and 1% P/S at 37°C. In some cases, cells transformed to expressed GFP and luciferase (231BR-GFP/Luc and 231BO-GFP/Luc) or mKate (231BO mKate) were used. Bt474m1 and Bt474m1-Br3 cells were maintained in RPMI medium supplemented with 10% FBS, 1% P/S, and 1% L-glut. Cells were passaged upon reaching 70-80% confluency, and media was changed every 2-3 days and 24 h before all zebrafish injections. Prior to injection, cells were washed with PBS and detached from the cell culture flask using 10 mM EDTA for 20 min at 37°C. Cells were resuspended in full growth medium, pelleted, resuspended in growth medium again, and counted. Cells were counted, centrifuged at 1000 rpm for 5 min, and resuspended in PBS containing CellTracker Deep Red (Cat. No. C34565, ThermoFisher) at 1 μM at a concentration of $2x10^6$ cells/ml and incubated at 37°C for 20-30 min. Stained cells were washed twice with PBS, with spins at 2000 rpm for 3 min between washes.

After the final spin, cells were resuspended to a concentration of 1 million cells/20 µl in PBS. For integrin-blocking experiments, the final resuspension solution contained 30 µg/ml IgG mouse isotype control (abcam ab91353) or anti-β1 integrin (abcam ab24693) antibody. Cells were kept on ice for 1-2 hours during injection, with at least 30 min incubation prior to the first injection.

Zebrafish circulatory injections

Tricaine stock was prepared by dissolving 400 mg of Tricaine powder (ethyl 3-aminobenzoate methanesulfonate; Cat. No. E10521-50G, Sigma Aldrich, St. Louis, MO, USA) with 97.9 ml of deionized water and 2.1 ml of 1 M Tris. Anesthetic fish water was prepared by mixing 4.2 ml of tricaine stock per 100 ml of fish water supplemented with PTU. For injection to the circulation, zebrafish were anesthetized in tricaine and oriented in a lateral orientation on an agarose bed. 2-5 nL of cells/PBS mixture where ~100 cells were injected directly in the circulation via the posterior cardinal vein using a pulled micropipette. For select experiments, 231BR-GFP/Luc and 231BO-mKate cells were incubated with 30 µg/ml IgG antibody, mixed in equal parts to obtain a total concentration of 1 million cells/20 µl in PBS, and co-injected directly to the zebrafish hindbrain. Injected fish were screened between 4-20 h post-injection to check for successful introduction of cells to the circulatory system prior to imaging or placement on the zebrafish husbandry system. Fish without cells in the circulation were euthanized.

Intravital microscopy

Zebrafish embryos (3 dpf) were anesthetized using a final concentration of 0.4% buffered tricaine dissolved in fish water that was supplemented with PTU as described above. Anesthetized fish were immobilized in 1% (w/v) low gelling temperature agarose (Cat. No. A9414-25G, Sigma

Aldrich) dissolved in fish water. To enable high-resolution confocal imaging of mounted embryos, fish were laterally oriented in coverglass-bottom chamber slides (Nunc Lab-Tek Chambered #1.0 Borosilicate Coverglass slides; Cat. No 155383, ThermoFisher Scientific, Waltham, MA, USA). PTU water supplemented with 0.4% buffered tricaine was then added to the imaging chamber to keep the embryos anesthetized over the course of the experiment.

To acquire images of motile cells, chamber slides containing the embryos were imaged on Zeiss 710 or 780 laser scanning confocal microscopes. One-photon, confocal, 2-dimensional images were acquired at lateral dimensions of 512 x 512 pixels, which were stacked to acquire 3-dimensional images of moving cells. Imaging conditions used were:

1. Tg(flk:mCherry/MRC1a:EGFP) zebrafish injected with 231BR or 231BO cells – cells were stained with Cell Tracker Deep Red prior to injection. Confocal z-stacks were acquired every 10 minutes for ~90 frames at 2 µm axial steps to image a total depth of ~150 µm. 12-bit images were acquired with a Zeiss 20x EC Plan-Neofluor, 0.3 NA objective and a digital zoom of 0.8, resulting in a field of view of 531.37 µm x 531.37 µm. Pinhole diameter was set at 90 µm. Samples were simultaneously excited with 488 nm light from an argon laser with a total power of 25 mW, 561 nm light from a solid-state laser with a total power of 20 mW, and 633 nm light from a HeNe633 solid state laser with a total power of 5 mW. Transmitted light was also recorded. Images were taken on two tracks to minimize signal overlap. All lasers were set at 2% total power. A beam splitter, MBS 488/561/633, was employed in the emission pathway to delineate the red (band-pass filters ~580-645 nm), green (band-pass filters ~493-574 nm), and far red (band-pass filters ~650-747 nm) channels. The master gain was set at or below 700 for

each channel. The zebrafish embryo was maintained at 33°C for the course of imaging. Pixel dwell times of 1.58 ms were used.

2. Tg(fli:EGFP) zebrafish were injected with 231BR or 231BO cells treated with 30 µg/ml of a function-blocking β1 integrin antibody or IgG control antibody. Cells were stained with CellTracker Deep Red prior to injection. Confocal z-stacks were acquired every 10 minutes for ~90 frames at 2 µm axial steps to image a total depth of ~150 µm. 12-bit images were acquired with a Zeiss Plan-Neofluor 10x/0.30 NA objective and a digital zoom of 1, resulting in a field of view of 850.19 µm x 850.19 µm. Pinhole diameter was set at 100 µm. Samples were simultaneously excited with 488 nm light from an argon laser with a total power of 25 mW and 633 nm light from a HeNe633 solid state laser with a total power of 5 mW. Transmitted light was also recorded. All lasers were set at 2% total power. A beam splitter, MBS 488/633, was employed in the emission pathway to delineate the green (band-pass filters ~493-598 nm) and far red (band-pass filters ~640-747 nm) channels. The master gain was set at or below 700 for each channel. The zebrafish embryo was maintained at 33°C for the course of imaging. Pixel dwell times of 1.58 ms were used.

To acquire high-resolution images of cells in the brain and CVP, tile scans of these regions were taken for laterally oriented, agarose mounted fish at 1, 2, and/or 5 dpi. One-photon, confocal, 2-dimensional images were acquired using the imaging tracks described above with a Zeiss 20x EC Plan-Neofluor objective and digital zoom of 1. No overlap was used in tile scans. Laser power was kept at or below 8% of total power for these images.

Quantification of the complexity of the zebrafish vasculature

Whole-embryo tile scans (15% tile overlap) of 2 dpf Tg(fli:EGFP) zebrafish were acquired on a Zeiss 780 LSM confocal microscope with a 20x Zeiss 20x EC Plan-Neofluor, 0.3 NA objective and a digital zoom of 1 using an axial step of 1 µm. Average intensity projections of the entire embryo were made. The line tool in Fiji was used to obtain widths of 10 vessels per fish in four fish in both the brain and ISV for a total of N=40 vessels at each location. To characterize vessel topographical complexity, the circle tool was used to draw 10, 20, 50, or 100 µm-diameter circular regions of interest. This region of interest was randomly placed over vessels in the brain, CVP, or ISV, and the Orientation J plugin in Fiji was used to measure the coherency (defined here as the order parameter) at each region of interest and is described in detail elsewhere(34). The order parameter ranged from a value of 0 for isotropic distributions to 1 for aligned regions. For each region of interest size and tissue (brain, CVP, or ISV), 10 regions were measured for 4 fish, giving a total number of N=40 regions.

Intravital cell tracking

Time-lapse microscopy images were exported to Fiji for analysis. To adjust for fish growth during imaging, images were first registered using the Correct 3D Drift plugin, with the vasculature of the fish used as a topographical reference. For registration, the multi-time scale computation, subpixel drift correction, and edge enhancement options were enabled. Cancer cells were tracked in 3D in registered images over a 12 h imaging window from the registered image stacks using the TrackMate plugin for Fiji. Images were segmented in the cancer cell fluorescence channel in each frame using a Laplacian of Gaussian (LoG) detector with a 15 µm estimated particle diameter. An initial threshold of 1.0 was set, and the sub-pixel localization and median filter options in TrackMate were activated. Segmentation was then further refined by manual

adjustment of the threshold to minimize detection of background objects. Segmented objects were linked from frame to frame with a Linear Assignment Problem (LAP) tracker with 30 µm maximum frame-to-frame linking distance. Tracks were visually inspected for completeness and accuracy over the entire acquisition period and were manually edited to ensure that point-to-point tracks were generated for the entire time that a cell was in the field of view.

Calculation of cell speed and residence time in the zebrafish

Cell tracks (x,y,t,z) were exported to MATLAB for analysis. For each cell, frame-to-frame speed was calculated by dividing the displacement of the cell by the time interval between frames. An average speed for that cell over the course of imaging was then calculated by averaging these frame-to-frame speeds, and that average speed was used in subsequent plots and calculations. Speeds were only calculated for those cells remaining in frame for at least 4 frames (30 min). Speeds plotted in Figure 2 are grouped measurements (231BR – 91 cells in brain, 131 cells in CVP; 231BO – 46 cells in brain, 56 cells in CVP) made from multiple fish (231BR – 6 embryos; 231BO – 8 embryos). Speeds were compared by 2-way ANOVA with Sidak's multiple comparisons post-test between cell types in each tissue. This is the same method used for tracking cells in the intersegmental vessels in vivo.

To calculate residence time in the brain and CVP, the number of frames that cells were tracked were simply counted and multiplied by the imaging interval (10 min) for observations made during the total analysis period, which was set at 72 frames. Cells that were in frame for only one frame were not considered. To estimate the percentage of cells becoming occluded in each tissue over this period, the number of cells present at the final frame was divided by the total number of cells observed for all fish. Resident times plotted in Figure 2 are grouped measurements

(231BR – 142 cells in brain, 230 cells in CVP; 231BO – 86 cells in brain, 97 cells in CVP) made from multiple fish (231BR – 7 embryos; 231BO – 10 embryos). Residence times and occlusion fractions were compared using two-way ANOVA with Tukey's multiple comparisons post-test carried out between all conditions. To determine the impact of blocking the function of β1 integrin, the average residence time and percentage of cells occluded in the 12 h window for cells treated with the function blocking antibody was divided by corresponding values for cells treated with the IgG isotype control antibody. Residence times and occlusion fractions were calculated from: 231BR IgG – 5 embryos, 207 cells in head, 159 cells in CVP; 231BR anti-β1 – 4 embryos, 181 cells I head, 296 cells in CVP; 231BO IgG – 5 embryos, 78 cells in head, 139 cells in CVP; anti-β1 – 3 embryos, 26 cells in head, 77 cells in CVP.

Quantification of cell numbers and extravasated cells in the zebrafish brain and CVP

Fish injected with cells were screened for health and successful dissemination of cells throughout the circulatory system prior to incubation at 33°C (2-4 dpf) and 28.5°C (4-7 dpf). At 5 dpi, fish were randomly selected from the husbandry tank, anesthetized, mounted in agarose, and imaged as described above. These fish were kept at 33°C from 1-2 dpi, unmounted and put up in individual tanks on a zebrafish system at 2 dpi and kept at 28.5°C until 5 dpi, when they were retrieved, mounted, and imaged. Feeding commenced at 5 dpf (3 dpi).

Cells were counted as being in the CVP if they were within or proximal to the cardinal artery and caudal vein plexus, from the first 15 intersegmental vessels to the end of the cardinal artery. Cells were counted as being in the brain if they were within the first 700 μm from the most distal location of arteries in the head. Cells in the heart sac, Duct of Cuvier, and aortic arches were not counted as being in the brain. The minimum size of particles in the deep red channel to be

counted as a cell was 10 μm x 10 μm, as determined by the size of the particle at the z slice of its largest diameter in Fiji. Cells were counted as extravasated if they were outside of the vessel lumen, judged by 3D volume reconstructions in Fiji. Cells were counted from N=18 fish for 231BR cell injections and N=22 fish for 231BO cell injections.

Microchannel experiments

Master molds for the microchannel devices were fabricated from SU-8 on silicon wafers using standard photolithographic techniques for dual-height structures. Two chrome-glass contact masks were designed using L-Edit (Mentor Graphics, Wilsonville OR) and purchased from Front Range Photomask (Lake Havasu City, AZ). Four-inch silicon wafers (NOVA Electronic Materials, Flower Mound, TX) were first cleaned with acetone, isopropanol, and water, then dehydrated for 10 minutes on a 200°C hotplate. Three layers of SU-8 photoresist (Microchem, Newton MA) were used to pattern the devices, with minor modifications of the manufacturer suggested protocols. First, an adhesion layer of SU-8 2000.5 was spun on the wafer using a single wafer spin coater (Model WS-650S-8NPP/LITE, Laurell Technologies, North Wales, PA), softbaked, flood-exposed with the mask aligner (Model 208, Optical Associates, Inc., San Jose, CA), and post-exposure baked. Second, the microchannel layer was patterned using the first chrome-glass mask with SU-8 2005 to make an array of 7 μm high, 8 μm wide channels; the SU-8 2005 layer was softbaked, exposed, and post-exposure baked. Both the SU-8 2000.5 and the SU-8 2005 were prepared in our laboratory by dilution of SU-8 2050 with SU-8 thinner (Microchem) to obtain the desired percent solids as per the manufacturer product sheets.

The large fluid channels were patterned with SU-8 2100 as received, using the second chrome-glass mask. Solvent edge bead removal was performed during the spinning step to ensure good contact between the mask and resist, and alignment marks were used to ensure the small microchannels were centered in the gap of the larger channels. For the thick layer, a long-pass filter (PL-360-LP, Omega Optical, Brattleboro, VT) was used during exposure to prevent overexposure of the top of the resist layer. After this final layer was softbaked, exposed, and post-exposure baked, the pattern was developed with SU-8 developer, rinsed thoroughly, and hardbaked at 150°C for two minutes. The templates were then treated with silane vapor (tridecafluoro-1,1,2,2-tetrahydrooctyl trichlorosilane (Gelest, Morrisville PA) for one hour to reduce adhesion during use.

Final microfluidic devices were formed using replica molding with polydimethylsiloxane (PDMS; Sylgard 184 kit, Dow Corning, Midland, MI, USA) at a ratio of 10 parts prepolymer to 1 part crosslinker. The PDMS components were mixed, poured over the patterned wafer, and degassed. PDMS devices were polymerized at 85°C for ~2 h before removal from the master mold. Devices were then cut, and fluid access ports were punched with 4 mm biopsy punches (Miltex, Electron Microscopy Sciences 69031-05).

PDMS devices were cleaned with ethanol and DI water. Devices and two-well coverglass-bottom chamber slides (Nunc Lab-Tek Chambered #1.0 Borosilicate Coverglass slides; Cat. No 155380, ThermoFisher Scientific, Waltham, MA, USA) were exposed to oxygen plasma for 30 sec. PDMS devices were then irreversibly bound to the slides and filled with PBS. Device walls were coated with 20 μg/ml rat tail collagen type I, 10 μg/ml fibronectin from human plasma (EMD Millipore, FC010), or 1% BSA (all dissolved in PBS) by adsorption for 1 h at 37°C, 5% CO_2.

Devices were washed with PBS following removal of the protein solution (**Supplementary Figure 4A**).

231BR and 231BO cells transformed to express green fluorescent protein (GFP) and luciferase (Luc), hereafter referred to as 231BR-GFP/Luc and 231BO-GFP/Luc, respectively, were washed with PBS, detached with 0.25% trypsin-EDTA, and resuspended in serum containing medium at $1x10^6$ cells/ml. Cells were introduced to the device by adding 20 µl of the cell seeding solution to the device inlet well, and the device was placed in the incubator for 15 min for cell attachment. If cell inlet flow stopped during this period, some of the seeding solution was moved to the other cell well to re-initiate flow. Following seeding, devices were washed by adding serum free medium to each well and incubating the device for 30 min. Devices were then washed three times using medium with serum. After the final wash, medium with serum was added to all wells, with an addition 2.5 ml/well of serum containing medium added to each well of the chamber slide to keep the device immersed and minimize evaporation during imaging. Thus, cells migrated in the device in the absence of flow and chemical gradients.

To obtain live cell images of migrating cells, devices were mounted in a stage top incubator on a Zeiss 780 LSM confocal microscope ~2 h after the final device wash. Devices were maintained at 37°C, 5% CO_2 and imaged every 10 min for up to 12 h using a Zeiss Plan-Neofluor 10x/0.30 NA objective and a digital zoom of 1, resulting in a field of view of 850.19 µm x 850.19 µm. Multiple positions were imaged to obtain fields of view encompassing the entire device. Samples were excited with 488 nm light from an argon laser with a total power of 25 mW to capture 2048 pixel x 2048 pixel, 16 bit, 2 line mean averaged images with the pinhole width set at 90 µm. The laser was set at 2% of total power. Biological duplicates were run for each combination

of cell type and ECM protein, with the exception of BSA, where three devices were analyzed for each cell type to obtain a sufficient number of cells in microchannels.

Calculation of cell speed from microchannel experiments

Migrating cells were tracked both within the microchannels and in the flat (2D) region of the device below the microchannels. To track cells, the GFP channel of each image was first preprocessed to better visualize cell morphology. In Fiji, the background was subtracted using the rolling ball method with a radius of 50 pixels. Images were then subjected to a Gaussian blur with sigma=2 pixels, following by an unsharp mask at a radius of 2 pixels and a mask value of 0.60. Processed images were saved as tiff files and tracked using TrackMate. Images were segmented using the Downsample LoG detector with a 40 µm estimated particle diameter, threshold of 0.1, and downsampling factor of 2. The entrance and exit of the microchannels was manually identified, and tracking was confined to either the regions where cells were fully within channels, or regions where cells did not interact with the microchannels (2D regions). Only tracks containing at least 12 points were retained for analysis. After initial track assignment using a LAP tracker, tracks were manually checked and updated for completeness and accuracy. Tracking was discontinued if a cell reached the end of a microchannel or exited the base of a microchannel, encountered a cell in the channel traveling in the opposite direction, or was in contact with a preceding cell in the microchannel.

Cell tracks (x,y,t,z) were exported to MATLAB for analysis. For each combination of cell type and ECM protein, 30 tracks were randomly selected, and an average speed for a given cell was obtained by averaging the frame-to-frame speed (calculated by dividing the displacement of the cell by the time interval between frames) over the first 30 frames for which the cell was tracked.

For BSA coated devices, fewer cells entered the microchannels, and fewer than 30 cells were used per biological repeat in some instances. Persistence ratio was defined as the total displacement of a cell over this same time period divided by the total distance traveled by the cell. Average speeds and persistence ratios were grouped from each biological replicate to obtain an ensemble of cell speeds and persistence ratios. This ensemble was averaged to obtain a mean cell migration speed and persistence for a given condition and analyzed across cell lines and ECM coatings by two-way ANOVA with Tukey's multiple comparisons post-test in GraphPad Prism 7.

Cell preparation for RNAseq and mass spectrometry

231BR or 231BO cells were washed with PBS and detached from cell culture flasks using 10 mM EDTA for 20 min at 37°C. Cells were resuspended in full growth medium, pelleted, resuspended in growth medium again, and counted. Cells were then centrifuged at 1000 rpm for 5 min and resuspended in PBS containing CellTracker Deep Red (Cat. No. C34565, ThermoFisher) at 1 μM at a concentration of $2x10^6$ cells/ml and incubated at 37°C for 20 min to match the preparation procedure used for *in vivo* injections. Stained cells were washed twice with PBS, with spins at 2000 rpm for 3 min between washes. After the final spin, cells were resuspended to a concentration of 1 million cells/20 µl in PBS. For the final resuspension, cells were in PBS containing 30 µg/ml IgG. Cells were incubated with the antibody for 30 min), diluted to a concentration of 1e6 cells/ml in serum free media, and seeded in 6-well plate wells (300,000 cells/well). Additional serum free media was added to bring the total volume in each well to 2 ml. Cells were incubated for 8 h at 37°C, 5% CO_2.

Mass spectrometry

Lysate was prepared by adding 40 µl/well of lysis buffer containing 1 part Calbiochem 539131 Protease inhibitor cocktail set 1, 1 part Sigma P5726 Phosphatase inhibitor cocktail 2, 1 part Sign P0044 phosphatase inhibitor cocktail 3, and 100 parts Thermo 78501 M-PER Mammalian Protein Extraction Reagent added. Cells were scraped, and lysate was collected. Lysate was sonicated 20 sec, spun down 5 min at 1600 rpm, and supernatant stored at -80°C prior to mass spectrometry. Lysates were prepared over three separate days to obtain biological triplicates.

Cell lysates (250 µg each) were digested with trypsin using the filter-aided sample preparation (FASP) protocol as previously described with minor modifications(60). Lysates were first reduced by incubation with 10 mM DTT at 55 °C for 30 min. Each lysate was then diluted with 8 M urea in 100 mM Tris-HCl (pH 8.5 [UA]) in a Microcon YM-10 filter unit and centrifuged at 14,000 × g for 30 min at 20°C. The lysis buffer was exchanged again by washing with 200 µL UA. The proteins were then alkylated with 50 mM iodoacetamide in UA, first incubated for 6 min at 25 °C and then excess reagent was removed by centrifugation at 14,000 × g for 30 min at 20°C. Proteins were then washed 3 × 100 µL 8 M urea in 100 mM Tris-HCl (pH 8.0) (UB). The remaining urea was diluted to 1 M with 100 mM Tris-HCl pH 8 and then the proteins were digested overnight at 37°C with trypsin at an enzyme to protein ratio of 1:100 w/w. Tryptic peptides were recovered from the filter by first centrifugation at 14,000 × g for 30 min at 20°C followed by washing of the filter with 50 µL 0.5 M NaCl. The peptides were acidified and desalted on a C18 SepPak cartridge (Waters) and dried by vacuum concentration (Labconco). Dried peptides were fractionated by high pH reversed-phase spin columns (Thermo). The peptides from each fraction were lyophilized, and dried peptides were solubilized in 4% acetonitrile and 0.5% formic acid in water for mass spectrometry analysis. Each fraction of each sample was separated on a 75 µm x 15 cm, 2 µm

Acclaim PepMap reverse phase column (Thermo) using an UltiMate 3000 RSLCnano HPLC (Thermo) at a flow rate of 300 nL/min followed by online analysis by tandem mass spectrometry using a Thermo Orbitrap Fusion mass spectrometer. Peptides were eluted into the mass spectrometer using a linear gradient from 96% mobile phase A (0.1% formic acid in water) to 35% mobile phase B (0.1% formic acid in acetonitrile) over 240 minutes. Parent full-scan mass spectra were collected in the Orbitrap mass analyzer set to acquire data at 120,000 FWHM resolution; ions were then isolated in the quadrupole mass filter, fragmented within the HCD cell (HCD normalized energy 32%, stepped ± 3%), and the product ions analyzed in the ion trap.

The mass spectrometry data were analyzed and label-free quantitation performed using MaxQuant version 1.5.7.4(61, 62) with the following parameters: variable modifications - methionine oxidation and N-acetylation of protein N-terminus; static modification – cysteine carbamidomethylation; first search was performed using 20 ppm error and the main search 10 ppm; maximum of two missed cleavages; protein and peptide FDR threshold of 0.01; min unique peptides 1; match between runs; label-free quantitation, with minimal ratio count 2. Proteins were identified using a Uniprot human database from November 2016 (20,072 entries). Statistical analysis was performed using Perseus version 1.5.6.0(63). After removal of contaminant and reversed sequences, as well as proteins that were only quantified in one of the three replicate experiments, the label-free quantitation values were base 2 logarithmized and missing values were imputed from a normal distribution of the data. Statistically significant differences were assigned using a two-way t-test with a p-value cut-off of 0.05. Hierarchical clustering was also performed in Perseus.

For analysis of protein expression and signaling pathways that were differentially regulated between the cell types, the annotated list of base 2 logarithmized values and p-values was imported

to Ingenuity Pathway Analysis. For comparison of 231BR and 231BO cells incubated with the IgG antibody prior to lysate collection, proteins were filtered to retain those with a p-value less than 0.05. This retained 526 of the total 2402 mapped proteins returned from Perseus analysis. Expression analysis was performed in IPA.

RNA-seq analysis

RNA isolation was performed using the PureLink RNA Mini Kit (Thermofisher 12183018A) according to the manufacturer's instructions and eluted in RNase-free water. Sequencing reads were trimmed for quality control using Trimmomatic (64) and quality was further verified with FASTQC (65). Trimmed reads were then aligned to human genome 19 (hg19) using STAR (66). Gene abundances were then determined using RSEM (67) and normalized with TMM (68). Differential expression between samples was then determined using EdgeR (69, 70) and visualized with ggplot2 (71).

Optical tweezer-based microrheology

For all experiments, at 24 hours post fertilization (hpf), embryos were transferred to egg water supplemented with phenylthiourea (PTU, Sigma P5272), suspended at 7.5% w/v in DMSO, at 1 part in 4500 to inhibit melanin formation for increased optical transparency. Embryos were then returned to the incubator at 28.5°C and checked for normal development. Zebrafish embryos at 2 days post fertilization (2 dpf) were anesthetized using 0.4% buffered tricaine. Polystyrene beads, 1 micron in diameter resuspended in PBS with a final cell concentration of 1×10^7 beads/ml, were injected directly into the organ of interest as previously described(35, 36). A subset was imaged 4 hours after injection, whereas the remainder were then reared at 28.5°C with 5% CO_2

and relative humidity maintained at 95% for two days. On the desired day of development, embryos were anesthetized using 0.4% buffered tricaine, then embedded in a lateral orientation in 1% low melting point agarose and allowed to polymerize in with cover glass (no. 1.5 thickness) as previously described (35). Egg water supplemented with tricaine was added to the agarose hydrogel for the entire time of data acquisition. For complete experimental details, see(35, 36, 72).

Our home-built setup consists of a 1064 nm trapping beam steered by an acousto-optic deflector to oscillate the trap and a stationary 975 nm detection beam that is coupled into and colocated with the trap with a dichroic before being sent into the backport of an inverted microscope with a long working distance water objective and a high NA condenser. Telescope lenses conjugate the optical plane at the acousto-optic deflector (AOD) to the back aperture of the condenser, which is placed in Kohler illumination after the object is focused in the specimen place. Above the condenser, the detection beam is relayed to a quadrant photodiode for back focal plane interferometric position detection. Each bead is positioned precisely in the center of the trap by scanning it through the detection beam in three dimensions using a piezo nanopositioning stage while recording the voltages from the QPD. The V-nm relation of the QPD is calibrated in situ by fitting the central linear region of the detector response to scanning the bead through the detection beam in the direction of the oscillations, giving β in V/nm . A second QPD records the position of the trapping laser to find the relative phase lag between the bead and trap oscillations. The optical trap stiffness k is determined in situ from the thermal power spectrum of each measured bead while the trap is stationary, using the active-passive calibration method(73). Together with β, k, and the bead's mass m and radius a, the trajectories yield the complex modulus as a function of frequency, G*(ω), of each bead's surrounding microenvironment. In this equation, the complex modulus, G*(ω), can be broken down into components, with $G^*(\omega) = G'(\omega) + iG''(\omega)$, where the real part,

G'(ω), is the elastic component and the imaginary part, G''(ω), is the viscous component. The complex modulus, G*(ω), is calculated as $G^*(\omega) = \frac{i\omega\tilde{\gamma}_D(\omega)}{6\pi a}$, where the friction relaxation spectrum $\tilde{\gamma}_D(\omega)$ is related by the equation $\tilde{\gamma}_D(\omega) + i\omega m = -\frac{k}{i\omega}\left(\frac{1}{i\omega\tilde{R}_L(\omega)} + 1\right)$ to the active power spectrum $\tilde{R}_L(\omega) \equiv \frac{\tilde{x}_{dr}(\omega)}{-i\omega\tilde{x}_L(\omega)}$, with $\tilde{x}_L(\omega)$ and $\tilde{x}_{dr}(\omega)$ the Fourier transforms of the time series of the positions of the trapping laser and the driven bead respectively, recorded while the trap is oscillating. The stiffness $k = \frac{\mathrm{Re}\{\tilde{R}_L(\omega)\}}{P_U(\omega)}$ is determined from the real part of the active power spectrum and the passive power spectrum, $P_U(\omega) \equiv \left\langle \left|\tilde{x}_U(\omega)\right|^2 \right\rangle$, where $\tilde{x}_U(\omega)$ is the Fourier transform of the time series of the undriven bead's thermally fluctuating position while the trap is held stationary. Each bead is subjected to fourteen consecutive 2s pulses, with the trap alternately oscillating or stationary. Amplitude of oscillations was set to 20nm with power of 100mW at the back aperture. Only probes at distances exceeding ~30 μm away from the cover slip surface to minimize drag in consideration of Faxen's law were measured (74).

Samples were measured in triplicate with at least 30 beads per sample measured. Laser power was set to 100mW at the back aperture. Data were analyzed using custom MATLAB programs. Experiments were controlled using custom LabVIEW programs. Active microrheology data are presented as complex modulus (mean ± standard deviation), normalized to the complex modulus of the CVP at either 2 dpf or 4 dpf. Data are also represented as a function of frequency from 3Hz to 15kHz. Data normalized to the complex modulus of the CVP were analyzed by two-way ANOVA with Tukey's honestly significant difference post-test.

REFERENCES

1. Nguyen DX, Bos PD, & Massague J (2009) Metastasis: from dissemination to organ-specific colonization. *Nat Rev Cancer* 9(4):274-284.
2. Obenauf AC & Massague J (2015) Surviving at a distance: organ specific metastasis. *Trends Cancer* 1(1):76-91.
3. Steeg PS (2016) Targeting metastasis. *Nat Rev Cancer* 16(4):201-218.
4. Paget S (1989) The distribution of secondary growths in cancer of the breast. 1889. *Cancer Metastasis Rev* 8(2):98-101.
5. Kennecke H*, et al.* (2010) Metastatic behavior of breast cancer subtypes. *J Clin Oncol* 28(20):3271-3277.
6. Steeg PS, Camphausen KA, & Smith QR (2011) Brain metastases as preventive and therapeutic targets. *Nat Rev Cancer* 11(5):352-363.
7. Tanner K & Gottesman MM (2015) Beyond 3D culture models of cancer. *Sci Transl Med* 7(283):283ps289.
8. Yoneda T, Williams PJ, Hiraga T, Niewolna M, & Nishimura R (2001) A bone-seeking clone exhibits different biological properties from the MDA-MB-231 parental human breast cancer cells and a brain-seeking clone in vivo and in vitro. *J Bone Miner Res* 16(8):1486-1495.
9. Zhang S*, et al.* (2013) SRC family kinases as novel therapeutic targets to treat breast cancer brain metastases. *Cancer Res* 73(18):5764-5774.
10. Condeelis J & Segall JE (2003) Intravital imaging of cell movement in tumours. *Nat Rev Cancer* 3(12):921-930.
11. Ewald AJ, Werb Z, & Egeblad M (2011) Dynamic, long-term in vivo imaging of tumor-stroma interactions in mouse models of breast cancer using spinning-disk confocal microscopy. *Cold Spring Harb Protoc* 2011(2):pdb top97.
12. Friedl P & Alexander S (2011) Cancer invasion and the microenvironment: plasticity and reciprocity. *Cell* 147(5):992-1009.
13. Hirata E*, et al.* (2015) Intravital imaging reveals how BRAF inhibition generates drug-tolerant microenvironments with high integrin beta1/FAK signaling. *Cancer Cell* 27(4):574-588.
14. Bissell MJ & Hines WC (2011) Why don't we get more cancer? A proposed role of the microenvironment in restraining cancer progression. *Nat Med* 17(3):320-329.
15. Kim J & Tanner K (2015) Recapitulating the Tumor Ecosystem Along the Metastatic Cascade Using 3D Culture Models. *Front Oncol* 5:170.
16. Kumar S & Weaver VM (2009) Mechanics, malignancy, and metastasis: the force journey of a tumor cell. *Cancer Metastasis Rev* 28(1-2):113-127.
17. Azevedo AS, Follain G, Patthabhiraman S, Harlepp S, & Goetz JG (2015) Metastasis of circulating tumor cells: favorable soil or suitable biomechanics, or both? *Cell Adh Migr* 9(5):345-356.
18. White R, Rose K, & Zon L (2013) Zebrafish cancer: the state of the art and the path forward. *Nat Rev Cancer* 13(9):624-636.
19. Stoletov K*, et al.* (2010) Visualizing extravasation dynamics of metastatic tumor cells. *J Cell Sci* 123(Pt 13):2332-2341.

20. Stoletov K, Montel V, Lester RD, Gonias SL, & Klemke R (2007) High-resolution imaging of the dynamic tumor cell vascular interface in transparent zebrafish. *Proc Natl Acad Sci U S A* 104(44):17406-17411.
21. Meeker ND & Trede NS (2008) Immunology and zebrafish: spawning new models of human disease. *Dev Comp Immunol* 32(7):745-757.
22. Oosterhof N, Boddeke E, & van Ham TJ (2015) Immune cell dynamics in the CNS: Learning from the zebrafish. *Glia* 63(5):719-735.
23. Murayama E*, et al.* (2006) Tracing hematopoietic precursor migration to successive hematopoietic organs during zebrafish development. *Immunity* 25(6):963-975.
24. Fleming A, Diekmann H, & Goldsmith P (2013) Functional characterisation of the maturation of the blood-brain barrier in larval zebrafish. *PloS one* 8(10):e77548.
25. Goessling W & North TE (2011) Hematopoietic stem cell development: using the zebrafish to identify the signaling networks and physical forces regulating hematopoiesis. *Methods in cell biology* 105:117-136.
26. Barnes JM, Przybyla L, & Weaver VM (2017) Tissue mechanics regulate brain development, homeostasis and disease. *J Cell Sci* 130(1):71-82.
27. Kienast Y*, et al.* (2010) Real-time imaging reveals the single steps of brain metastasis formation. *Nat Med* 16(1):116-122.
28. Mathura KR*, et al.* (2001) Comparison of OPS imaging and conventional capillary microscopy to study the human microcirculation. *Journal of applied physiology (Bethesda, Md. : 1985)* 91(1):74-78.
29. Tufto I & Rofstad EK (1999) Interstitial fluid pressure and capillary diameter distribution in human melanoma xenografts. *Microvascular research* 58(3):205-214.
30. Doerschuk CM, Beyers N, Coxson HO, Wiggs B, & Hogg JC (1993) Comparison of neutrophil and capillary diameters and their relation to neutrophil sequestration in the lung. *Journal of applied physiology (Bethesda, Md. : 1985)* 74(6):3040-3045.
31. Potter RF & Groom AC (1983) Capillary diameter and geometry in cardiac and skeletal muscle studied by means of corrosion casts. *Microvascular research* 25(1):68-84.
32. Watkins SC*, et al.* (2012) High resolution imaging of vascular function in zebrafish. *PloS one* 7(8):e44018.
33. Oudin MJ & Weaver VM (2016) Physical and Chemical Gradients in the Tumor Microenvironment Regulate Tumor Cell Invasion, Migration, and Metastasis. *Cold Spring Harb Symp Quant Biol* 81:189-205.
34. Fonck E*, et al.* (2009) Effect of aging on elastin functionality in human cerebral arteries. *Stroke* 40(7):2552-2556.
35. Blehm BH, Devine A, Staunton JR, & Tanner K (2016) In vivo tissue has non-linear rheological behavior distinct from 3D biomimetic hydrogels, as determined by AMOTIV microscopy. *Biomaterials* 83:66-78.
36. Staunton JR, Blehm B, Devine A, & Tanner K (2017) In situ calibration of position detection in an optical trap for active microrheology in viscous materials. *Opt Express* 25(3):1746-1761.
37. Staunton JR*, et al.* (2016) Mechanical properties of the tumor stromal microenvironment probed in vitro and ex vivo by in situ-calibrated optical trap-based active microrheology. *Cell Mol Bioeng* 9(3):398-417.

38. Tanner K, Mori H, Mroue R, Bruni-Cardoso A, & Bissell MJ (2012) Coherent angular motion in the establishment of multicellular architecture of glandular tissues. *Proc Natl Acad Sci U S A* 109(6):1973-1978.
39. Weaver VM*, et al.* (1997) Reversion of the malignant phenotype of human breast cells in three-dimensional culture and in vivo by integrin blocking antibodies. *J Cell Biol* 137(1):231-245.
40. Patsialou A*, et al.* (2009) Invasion of human breast cancer cells in vivo requires both paracrine and autocrine loops involving the colony-stimulating factor-1 receptor. *Cancer Res* 69(24):9498-9506.
41. Wyckoff JB*, et al.* (2007) Direct visualization of macrophage-assisted tumor cell intravasation in mammary tumors. *Cancer Res* 67(6):2649-2656.
42. Sacco A*, et al.* (2016) Cancer Cell Dissemination and Homing to the Bone Marrow in a Zebrafish Model. *Cancer Res* 76(2):463-471.
43. Renshaw SA & Trede NS (2012) A model 450 million years in the making: zebrafish and vertebrate immunity. *Dis Model Mech* 5(1):38-47.
44. Nombela-Arrieta C*, et al.* (2013) Quantitative imaging of haematopoietic stem and progenitor cell localization and hypoxic status in the bone marrow microenvironment. *Nature cell biology* 15(5):533-543.
45. Ramasamy SK*, et al.* (2016) Blood flow controls bone vascular function and osteogenesis. *Nature communications* 7:13601.
46. Kusumbe AP, Ramasamy SK, & Adams RH (2014) Coupling of angiogenesis and osteogenesis by a specific vessel subtype in bone. *Nature* 507(7492):323-328.
47. Ma D, Zhang J, Lin HF, Italiano J, & Handin RI (2011) The identification and characterization of zebrafish hematopoietic stem cells. *Blood* 118(2):289-297.
48. Hanahan D & Weinberg RA (2011) Hallmarks of cancer: the next generation. *Cell* 144(5):646-674.
49. Fidler IJ (2003) The pathogenesis of cancer metastasis: the 'seed and soil' hypothesis revisited. *Nat Rev Cancer* 3(6):453-458.
50. Nguyen-Chi M*, et al.* (2015) Identification of polarized macrophage subsets in zebrafish. *eLife* 4:e07288.
51. Balzer EM*, et al.* (2012) Physical confinement alters tumor cell adhesion and migration phenotypes. *FASEB journal : official publication of the Federation of American Societies for Experimental Biology* 26(10):4045-4056.
52. Mathieu E*, et al.* (2016) Time-lapse lens-free imaging of cell migration in diverse physical microenvironments. *Lab on a chip* 16(17):3304-3316.
53. Kniazeva E*, et al.* (2012) Quantification of local matrix deformations and mechanical properties during capillary morphogenesis in 3D. *Integr Biol (Camb)* 4(4):431-439.
54. Kotlarchyk MA*, et al.* (2011) Concentration independent modulation of local micromechanics in a fibrin gel. *PloS one* 6(5):e20201.
55. Schwartz MA (2010) Integrins and extracellular matrix in mechanotransduction. *Cold Spring Harb Perspect Biol* 2(12):a005066.
56. Chen MB, Lamar JM, Li R, Hynes RO, & Kamm RD (2016) Elucidation of the Roles of Tumor Integrin beta1 in the Extravasation Stage of the Metastasis Cascade. *Cancer Res* 76(9):2513-2524.

57. Hoshino A*, et al.* (2015) Tumour exosome integrins determine organotropic metastasis. *Nature* 527(7578):329-335.
58. Jung HM*, et al.* (2017) Development of the larval lymphatic system in zebrafish. *Development* 144(11):2070-2081.
59. Lawson ND & Weinstein BM (2002) In vivo imaging of embryonic vascular development using transgenic zebrafish. *Developmental biology* 248(2):307-318.
60. Wisniewski JR, Zougman A, Nagaraj N, & Mann M (2009) Universal sample preparation method for proteome analysis. *Nature methods* 6(5):359-362.
61. Cox J*, et al.* (2014) Accurate proteome-wide label-free quantification by delayed normalization and maximal peptide ratio extraction, termed MaxLFQ. *Molecular & cellular proteomics : MCP* 13(9):2513-2526.
62. Cox J & Mann M (2008) MaxQuant enables high peptide identification rates, individualized p.p.b.-range mass accuracies and proteome-wide protein quantification. *Nature biotechnology* 26(12):1367-1372.
63. Tyanova S*, et al.* (2016) The Perseus computational platform for comprehensive analysis of (prote)omics data. *Nature methods* 13(9):731-740.
64. Bolger AM, Lohse M, & Usadel B (2014) Trimmomatic: a flexible trimmer for Illumina sequence data. *Bioinformatics* 30(15):2114-2120.
65. Andrew S (2010) FastQC: a quality control tool for high throughput sequence data).
66. Dobin A*, et al.* (2013) STAR: ultrafast universal RNA-seq aligner. *Bioinformatics* 29(1):15-21.
67. Li B & Dewey CN (2011) RSEM: accurate transcript quantification from RNA-Seq data with or without a reference genome. *BMC Bioinformatics* 12:323.
68. Robinson MD & Oshlack A (2010) A scaling normalization method for differential expression analysis of RNA-seq data. *Genome Biol* 11(3):R25.
69. McCarthy DJ, Chen Y, & Smyth GK (2012) Differential expression analysis of multifactor RNA-Seq experiments with respect to biological variation. *Nucleic Acids Res* 40(10):4288-4297.
70. Robinson MD, McCarthy DJ, & Smyth GK (2010) edgeR: a Bioconductor package for differential expression analysis of digital gene expression data. *Bioinformatics* 26(1):139-140.
71. Wickham H (2009) *ggplot2: Elegant Graphics for Data Analysis* (Springer-Verlag New York).
72. Staunton JR*, et al.* (2016) Mechanical properties of the tumor stromal microenvironment probed in vitro and ex vivo by in situ-calibrated optical trap-based active microrheology. *Cellular and molecular bioengineering* 9(3):398-417.
73. Fischer M & Berg-Sørensen K (2007) Calibration of trapping force and response function of optical tweezers in viscoelastic media. *Journal of Optics A: Pure and Applied Optics* 9(8):S239.
74. Neuman KC & Block SM (2004) Optical trapping. *Rev Sci Instrum* 75(9):2787-2809.

FIGURES

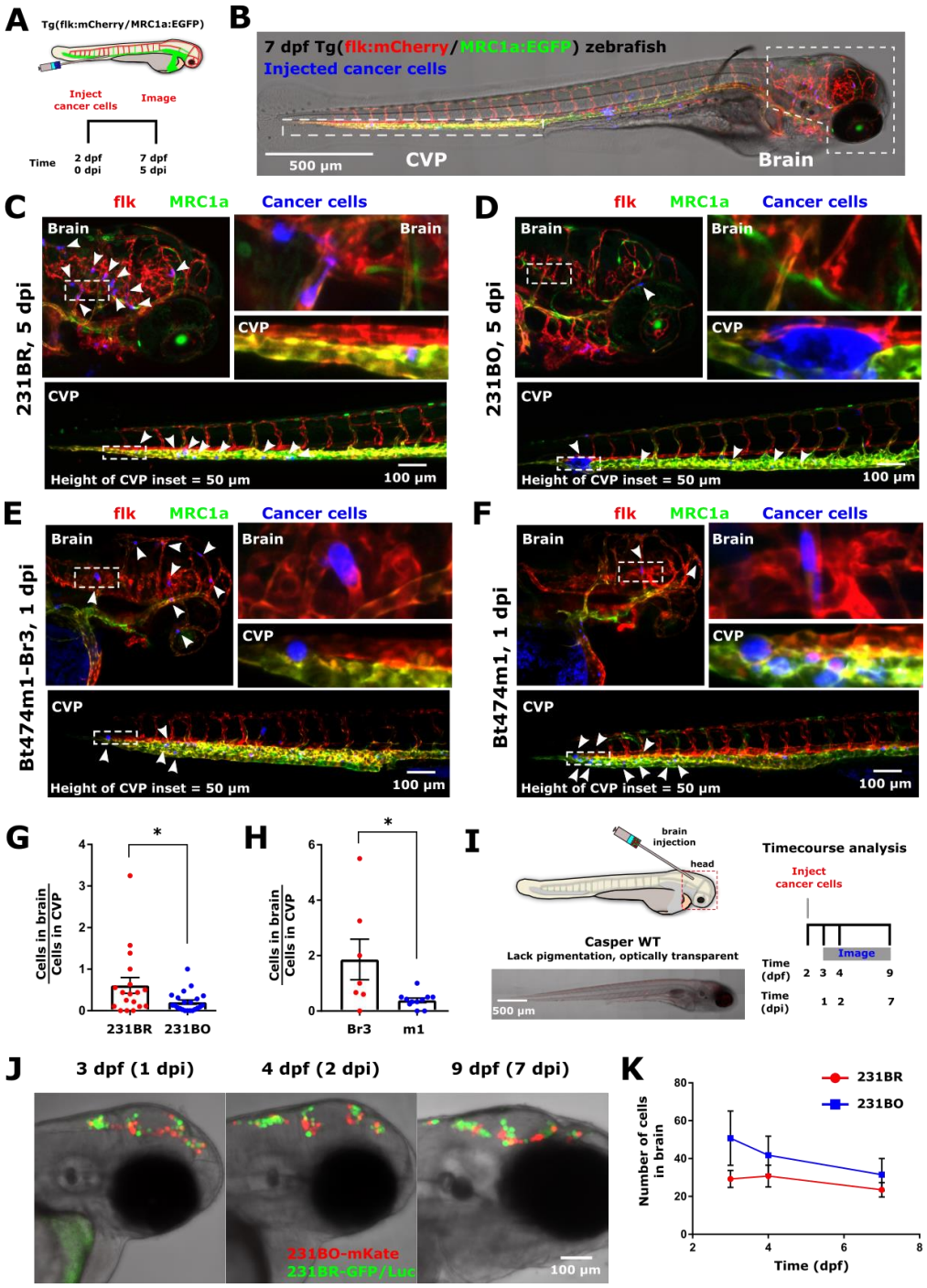

Figure 1. Non-random targeting of organ-tropic human cell lines in a zebrafish metastasis model. (A) Schematic of experimental setup. Cancer cells were injected into the circulatory system of Tg(flk:mCherry/MRC1a:EGFP) zebrafish at 2 days post-fertilization (dpf) and imaged at 5 days

post-injection (dpi; zebrafish age at imaging was 7 dpf). (B) Overview (average intensity projection from confocal z stack) of 7 dpf zebrafish. The brain and CVP are outlined. Scale is indicated. Representative images of (C) 231BR and (D) 231BO colonization in the zebrafish brain and CVP at 5 dpi. Inset locations are indicated on the top left and bottom panels. Arrows indicate cell positions. For scale, the height of the CVP inset = 50 μm. Representative images of (E) Bt474m1-Br3 and (F) Bt474m1 cells at 1 dpi. (G) Ratio of 231BR and 231BO cell numbers in the brain to CVP at 5 dpi following circulatory injection (mean ± SEM). *, $p<0.05$ by Mann-Whitney test. N=18 zebrafish injected with 231BR cells, N=22 zebrafish injected with 231BO cells. (H) Ratio of Bt474m1-Br3 and Bt474m1 cell numbers in the brain to CVP at 1 dpi following circulatory injection (mean ± SEM). *, $p<0.05$ by Mann-Whitney test. N=7 zebrafish injected with Bt474m1-Br3 cells, N=11 zebrafish injected with Bt474m1 cells. (I) Schematic of direct brain injection experiments. 231BR-GFP/Luc and 231BO-mKate were co-injected into the brain of non-pigmented Casper WT zebrafish. A representative image of the fish at 7 dpi (9 dpf) is shown. Fish were imaged at 1, 2, and 7 dpi, and total cell numbers were counted on each day. (J) Representative images of a brain-injected Casper WT larvae over the imaging period. The same fish imaged over multiple sessions is shown. (K) Numbers of 231BR and 231BO cells present over time following co-injection to the brain. Plot displays mean ± SEM cells from N=4 injected zebrafish.

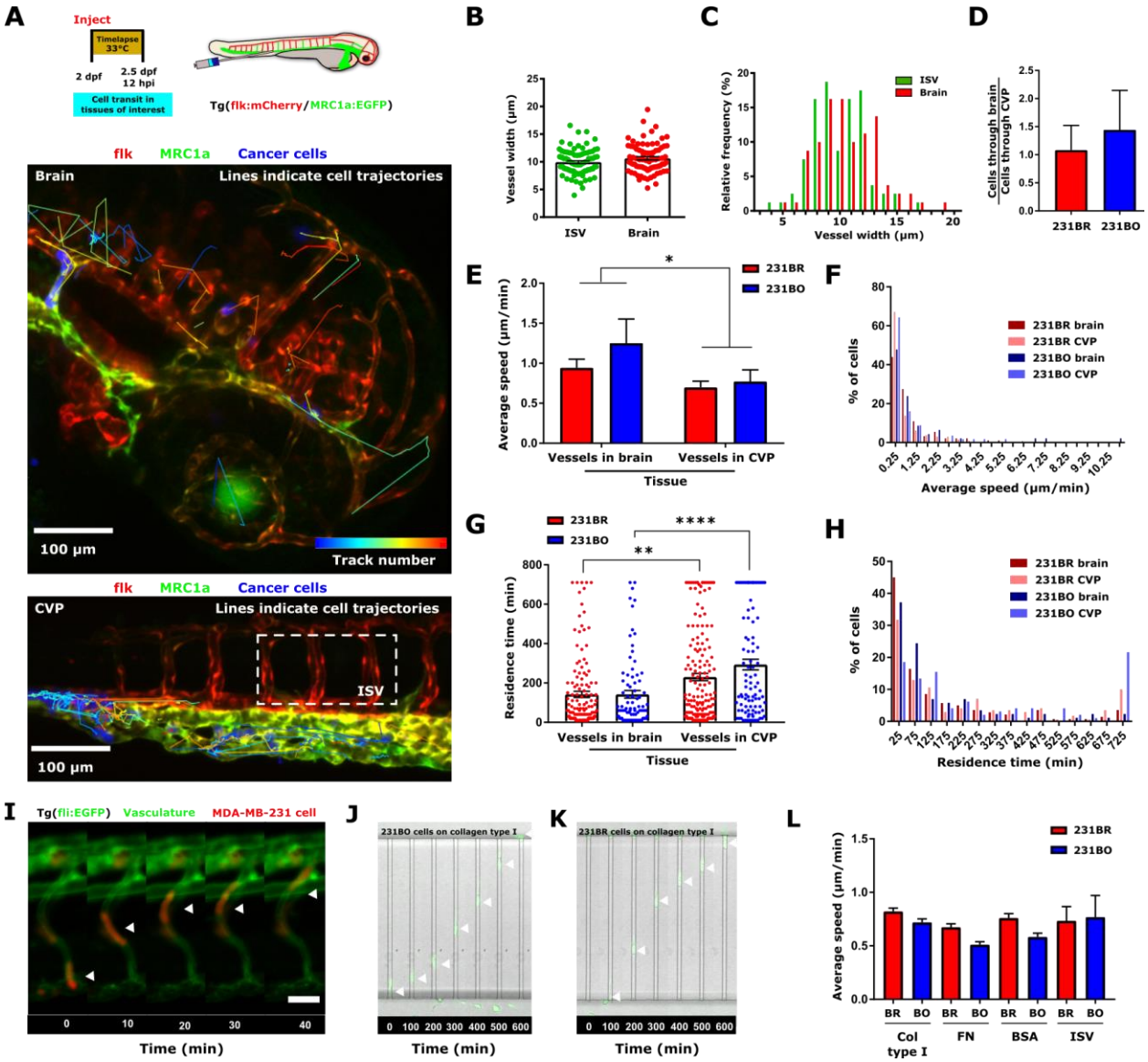

Figure 2. Cell speed in zebrafish organs is regulated by vessel architecture. (A) Schematic and representative results of vascular trafficking experiment. Tg(flk:mCherry/MRC1a:EGFP) zebrafish were injected with 231BR or 231BO cells in the dorsal aorta. The brain and CVP were then imaged for 12 h post-injection to visualize cell arrival and arrest within multiple tissues of the same fish. Representative images of cell trajectories within the zebrafish brain and CVP are shown. Trajectories are overlaid on the 12 h image. Tracks are pseudocolored by track number (blue=first track, red=final track). Scale bar = 100 µm. (B) Average ± SEM and (C) distribution of blood

vessel widths in the zebrafish intersegmental vessels (ISV) and brain. Vessels were measured from four Tg(fli:EGFP) zebrafish at 2 dpf, 20 vessels per region/fish, to obtain a total of N=80 vessels at each location. (D) Ratio of cells tracked in the brain to cells tracked in the CVP for both 231BR and 231BO cells. Plot displays mean ± SEM for this ratio averaged across N=7 fish for 231BR cells and N=10 fish for 231BO cells. (E) Average speeds and (F) distribution of speeds of 231BR and 231BO cells trafficking through the brain and CVP. *, $p<0.05$ by two-way ANOVA, with tissue as a significant source of variation. (G) Average residence times and (H) distribution of residence times of 231BR and 231BO cells trafficking through the brain and CVP. **, $p<0.01$; ****, $p<0.0001$ by two-way ANOVA with Tukey's multiple comparisons post-test. (I) Image of MDA-MB-231 cell (red) migrating through zebrafish intersegmental vessel (green). Arrow indicates cell location. Time-lapse images of (J) 231BO-GFP/Luc and (K) 231BR-GFP/Luc cell migration through confining microchannels coated with 20 μg/ml collagen type I. Arrows indicate cell position. (L) Average speeds (mean ± SEM) of cells migrating in microchannels and zebrafish intersegmental vessels. **, $p<0.01$ by one-way ANOVA with Dunn's post-test. In the microchannels, speeds from at least 52 cells collected over at least 2 biological duplicates were measured. Speeds in the intersegmental vessels were measured for N=38 231BR cells and N=14 231BO cells.

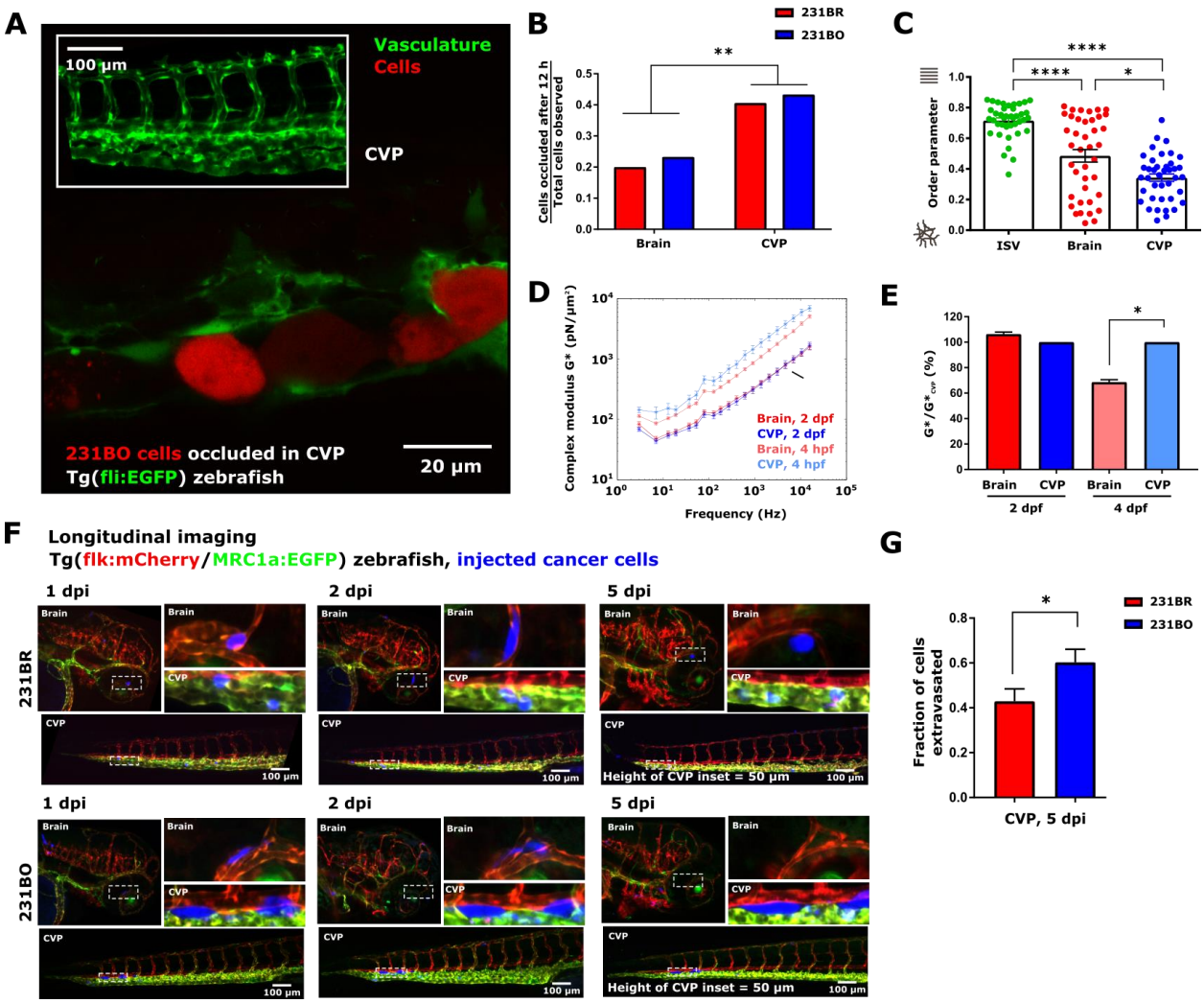

Figure 3. Topographical and emergent determinants of organ selectivity in the zebrafish. (A) Image of 231BO cells occluded in the CVP of a 2 dpf Tg(fli:EGFP) zebrafish ~4 h post-injection to the zebrafish circulation. (B) Fraction of cells occluded in the brain and CVP after 12 h of tracking to the total cells tracked in each organ. Data are collected from N=7 zebrafish for 231BR cells and N=10 zebrafish for 231BO cells. **, $p<0.01$, with tissue but not cell type a significant source of variation by two-way ANOVA. (C) Order parameter characterizing the topography of vessels in the ISV, brain, and CVP over 20 µm-diameter regions of interest. A value of 1 indicates aligned structures, while a value of 0 indicates isotropic structures. Vessels were measured from

four Tg(fli:EGFP) zebrafish at 2 dpf, 10 regions per tissue/fish, to obtain a total of N=40 vessels at each location. *, $p<0.05$; ****, $p<0.0001$ by Dunn's multiple comparisons post-test. (D) Complex modulus as a function of frequency in the brain and CVP at 2 dpf and 4 dpf. Arrow indicates proximity of values in the brain and CVP at 48 dpf. (E) Mean complex modulus in the brain and 2 dpf and 4 dpf, normalized to the mean complex modulus in the CVP on the same day. *, $p<0.05$ by Tukey's honestly significant difference test following two-way ANOVA. (F) Longitudinal imaging of Tg(flk:mCherry/MRC1a:EGFP) zebrafish injected in the dorsal aorta at 2 dpf with 231BR or 231BO cells. Fish were imaged at 1, 2, and 5 dpi to visualize cell numbers and extravasation status in the brain and CVP. Inset locations are indicated on the top left and bottom panels. Arrows indicate cell positions. For scale, the height of the CVP inset = 50 μm. (G) Fraction of cells present that were extravasated in the CVP at 5 dpi for 231BR and 231BO cells. *, $p<0.05$ by unpaired t-test. N=18 zebrafish injected with 231BR cells, N=22 zebrafish injected with 231BO cells.

A Differentially regulated genes

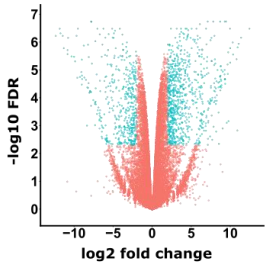

Gene	Fold Change	FDR
ITGA2	2.1	0.0013
ITGA3	2.3	0.0014
ITGA6	1.7	0.011
VCL	1.8	0.0060
ZYX	1.7	0.0021
PXN	1.6	0.0085
ROCK1	1.5	0.0027
ROCK2	1.4	0.014

B Differentially regulated proteins

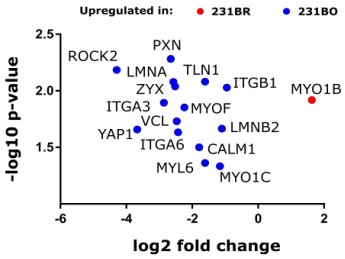

C Top differentially regulated canonical pathways

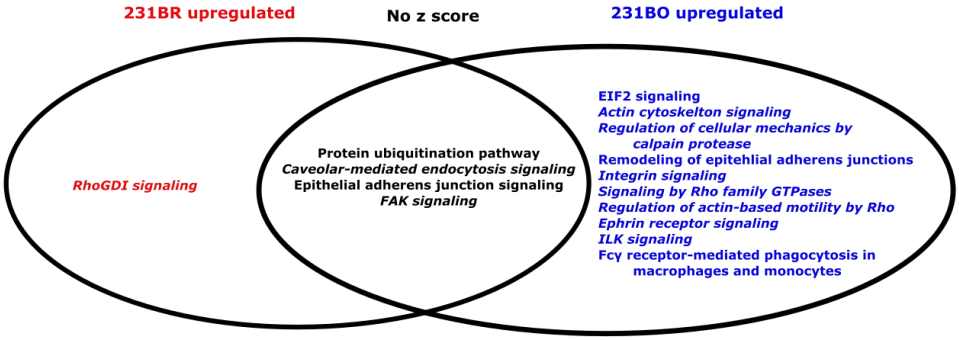

β1 integrin involvement: 10 of 15 most differentially regulated canonical pathways

D IgG

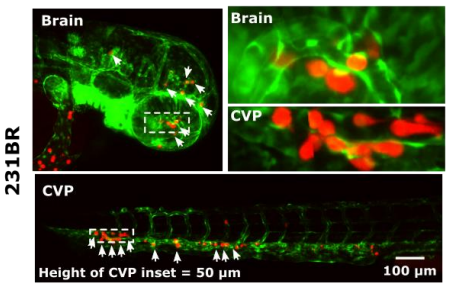

E anti-β1

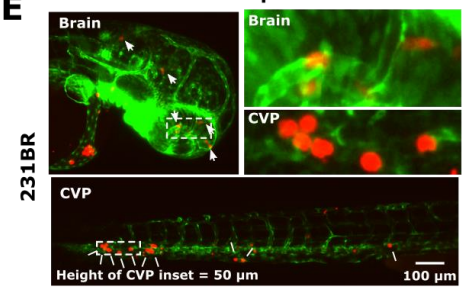

F

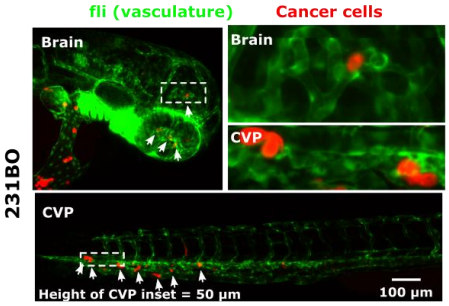

G

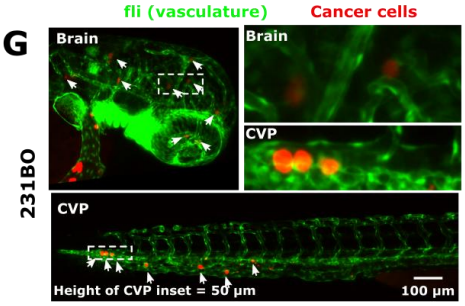

H

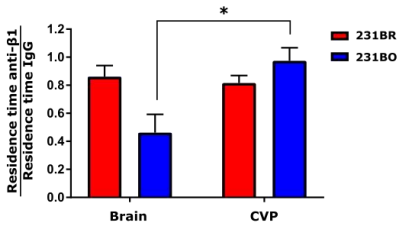

I

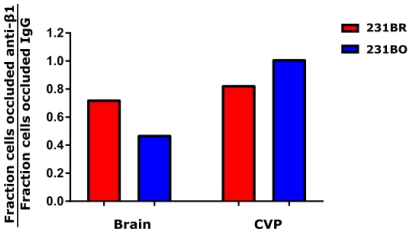

Figure 4. Initial cell trafficking to the zebrafish brain is mediated by β1 integrin activity. (A) Volcano plot of differentially expressed genes between 231BR and 231BO cells. Genes that had a false discovery rate (FDR) of FDR < 0.005 and a log2 fold change > 2.0 are shown in blue (1,297 genes), genes not meeting these criteria are shown in red (26,964 genes). A table of differentially regulated genes involved with focal adhesions and cell contractility is also provided. (C) List of the top differentially regulated canonical signaling pathways between 231BR and 231BO cells from pathway analysis of mass spectrometry data. Where possible, the direction of pathway regulation (from analysis z score) is indicated. Pathways in which β1 integrin is implicated are italicized. Representative images of 231BR cells treated with (D) IgG control or (E) function blocking antibody against β1 integrin and 231BO cells treated with (F) IgG control or (G) function blocking antibody against β1 integrin approximately 4 h after injection to 2 dpf Tg(fli:EGFP) zebrafish. Inset locations are indicated on the top left and bottom panels. Cells are displayed in red, and the vasculature is displayed in green. Arrows indicate cell positions. For scale, the height of the CVP inset = 50 μm. (H) Residence times (mean ± SEM) of 231BR and 231BO cells treated with β1 integrin function blocking antibody in the brain and CVP, normalized by the average residence time of the same cell type treated with an IgG isotype control antibody in the same tissue. *, $p<0.05$ by Sidak's multiple comparisons test between the same cell type following two-way ANOVA. (I) Fractional change in cell occlusion in each organ and for each cell type upon inhibition of β1 integrin. Fraction of cells present in each tissue after 12 h of tracking to total number of cells tracked were normalized to the fraction of the same cell type occluded upon treatment with IgG isotype control antibody.

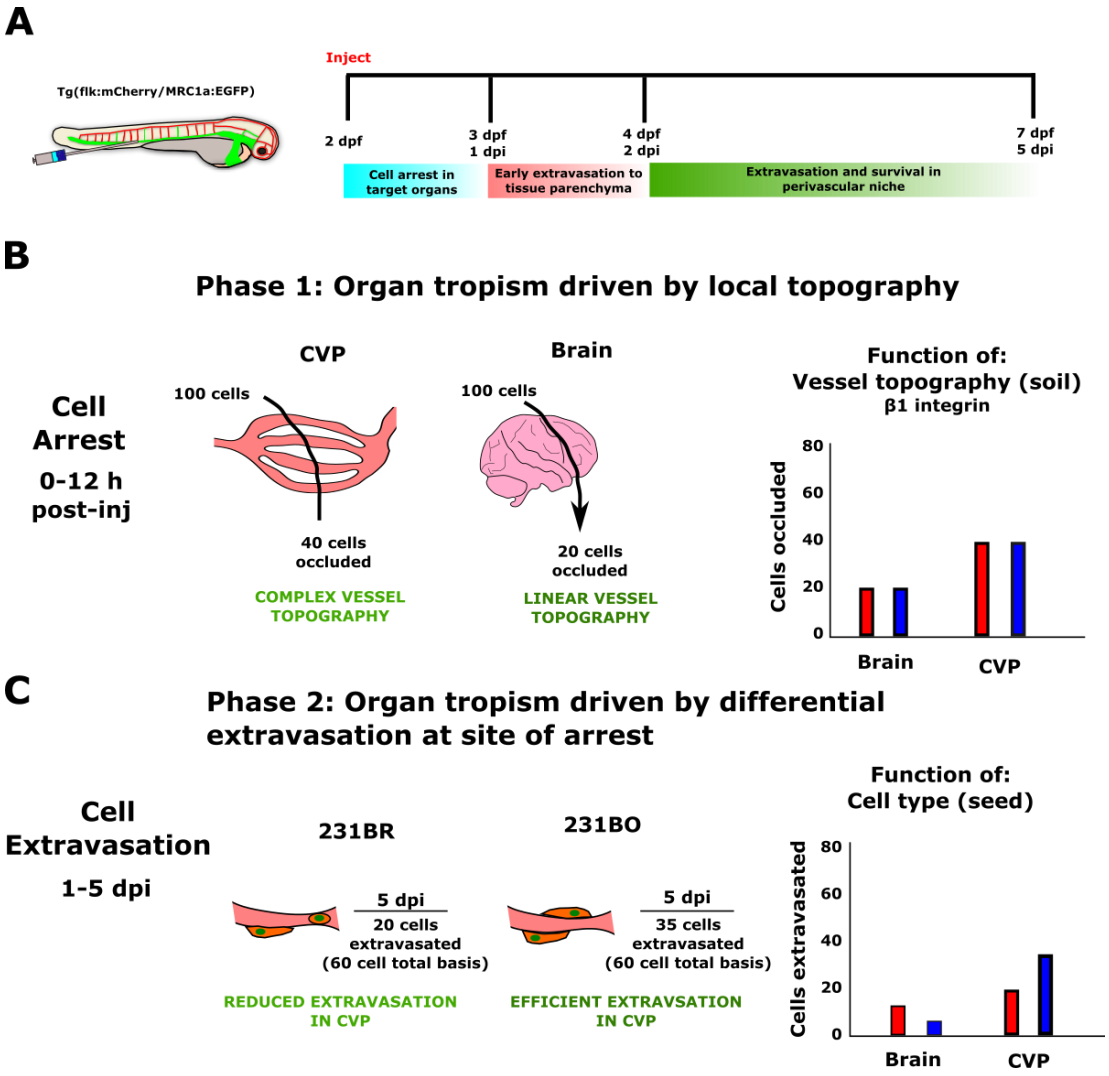

Figure 5. Model of non-random organ targeting in the embryonic zebrafish model. (A) Schematic of cell arrest and extravasation. Following injection at 2 dpf, cells arrest over the first 12-24 h after injection. Cells then extravasate from blood vessels and survive in perivascular positions in the tissue parenchyma. (B) Model of non-random organ targeting by differential cell arrest during early dissemination. Regardless of cell type, approximately 40% of cells observed arrested in the CVP over the first 12 h following injection, while approximately 20% of cells observed arrested in the brain. Arrest was at least partially dependent on β1 integrin function but was primarily driven by tissue/vascular architecture. Plots are drawn on a basis of 100 cells observed per tissue. (C) Model of extravasation leading to non-random organ targeting following

extravasation. Following arrest, 231BO cells extravasated more efficiently in the CVP than 231BR cells, leading to an increase in the relative number of 231BR cells in the brain by 5 dpf. Plot is drawn on the basis of 60 total cells present at 5 dpi.